Mueller matrix bidirectional reflectance distribution function measurements and modeling of textured silicon surfaces

Thomas A. Germer[a], Martin Foldyna[b,c], Zuzana Mrazkova[b,d],
Guillaume Fischer[c], and Etienne Drahi[c,e]

[a]Sensor Science Division, National Institute of Standards and Technology, Gaithersburg, Maryland 20899 USA
[b]LPICM-CNRS (Laboratoire de Physique des Interfaces et des Couches Minces – Centre National de la Recherche Scientifique), Ecole Polytechnique, Université Paris-Saclay, 91128 Palaiseau, France
[c]IPVF (Institut Photovoltaïque d'Ile-de-France), 8 rue de la Renaissance, 92160 Antony, France
[d]Nanotechnology Centre and Department of Physics, Technical University of Ostrava, 708 33, Ostrava-Poruba, Czech Republic
[e]TOTAL – New Energies, 24 cours Michelet, 92078 Paris La Défense, France

ABSTRACT

Surface texturing plays an important role in trapping light in photovoltaic materials. Understanding and modeling diffuse scatter from various textured silicon surfaces should aid in increasing light trapping in these materials, as well as improving material characterization and inspection during manufacture. We have performed Mueller matrix bidirectional reflectance distribution function (BRDF) measurements from a variety of textured silicon surfaces. Simulations, using multiple reflection polarization ray tracing, reproduce many of the features in the data. Evidence for diffraction, however, can also be observed, suggesting that a purely ray-tracing approach is insufficient for accurately describing the scatter from these materials.

Keywords: BRDF, Mueller matrix, photovoltaics, pyramids, scattering, surface texture

1. INTRODUCTION

Surface texturing is often used to increase absorption of light in photovoltaic materials. [1] The texture serves two functions: it reduces the reflectance by allowing incident radiation to reflect multiple times, and it diffuses the radiation within the material, so that weakly absorbing radiation experiences an enhanced path length to improve absorption. Besides geometrically increasing the path length inside the material, obliquely propagating radiation will experience total internal reflection at the interfaces, further trapping the radiation. Yablonovitch determined that the path length enhancement afforded by enhanced trapping can be as high as $4n^2$ for a random texture, where n is the index of refraction. [2, 3]

Characterization of surface texturing is needed during solar cell fabrication and can be performed rapidly by optical scattering measurements. [4, 5] While intensity measurements alone may be sufficient to provide pass/fail determination, more rigorous measurements using polarimetry may yield secondary information that helps to identify process failure modes. However, unless one resorts to a signature-based or process-experience method, an understanding of the scattering mechanisms and how the texture affects the scatter distribution and polarization is needed.

In this study, we performed optical scattering measurements from textured silicon surfaces, in order to better understand the propagation of radiation from these surfaces. While one of the research goals is to better understand the optical trapping characteristics at long wavelengths, these were reflectance measurements performed at a wavelength where the material is opaque. Nonetheless, the results demonstrate the usefulness of light scattering for characterizing these surfaces.

We will describe the measurement techniques in Sec. 2. In Sec. 3, we describe the samples that we performed the measurements on. Section 4 describes the ray models used and how diffraction would be expected to play a role. The results, together with discussion, will be given in Sec. 5. Finally, in Sec. 6, we will make some concluding remarks.

2. MEASUREMENT METHODS

2.1 Instrument

All of the measurements shown in this paper were performed at a wavelength of 633 nm, using a HeNe laser and the Goniometric Optical Scatter Instrument (GOSI). [6] This laser-based scatterometer can measure the Mueller matrix bidirectional reflectance distribution function (BRDF) for nearly any pair of incident and viewing directions, including those out of the plane of incidence. The incident direction $\hat{\mathbf{k}}_\mathrm{i}$ is parameterized by spherical coordinates with polar angle θ_i and azimuthal angle ϕ_i, while the viewing direction $\hat{\mathbf{k}}_\mathrm{r}$ is parameterized with a polar angle θ_r and azimuthal angle ϕ_r. Restrictions include some directions with polar angles greater than 75°, dependent upon all four angles, because of the presence of a rotation stage, and for directions within 5° of the retroreflection direction, because of the size of the receiver. The receiver has a precision aperture subtending approximately $\Omega = 1.15 \times 10^{-4}$ sr, a focusing lens, a rotating retarder, a polarizer, and an integrating sphere. The integrating sphere has a Si photodiode and a photomultiplier tube. However, for the measurements described here, the scattering levels were high enough that only the Si photodiode was used. The incident laser beam is fixed and horizontal, while the receiver rotates in a horizontal plane. The BRDF, f_r, is determined from

$$\Phi_\mathrm{r} = f_\mathrm{r}\, \Phi_\mathrm{i}\, \Omega \cos\theta_\mathrm{r}\,, \tag{1}$$

where Φ_r is the scattered radiant flux, and Φ_i is the incident radiant flux, measured with the sample removed and the receiver in the incident beam. The measurement sequence consisted of two hemispherical scans, described in Sec. 2.2, and two retroreflective scans, described in Sec. 2.3.

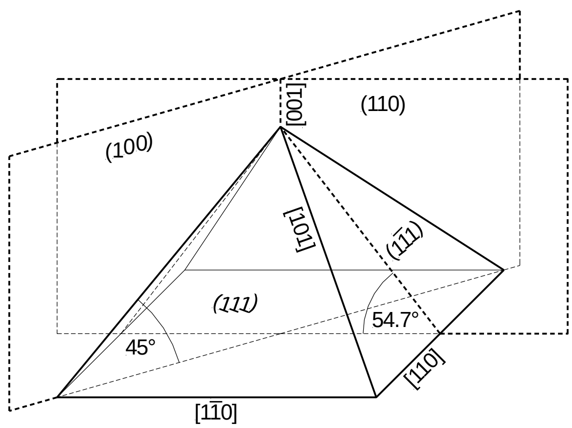

Figure 1. A pyramid on a (001) silicon surface, shown as solid lines, showing various directions (in brackets), planes (in parentheses), and angles. The two incident planes, (110) and (100), used in the measurements are shown with dashed lines.

2.2 Hemispherical BRDF measurements

Measurements of the BRDF were performed for two incident angles, θ_i=5° and 60°, where the incident plane is the (110) Si crystal plane, which includes the $[1\bar{1}0]$ and $[001]$ crystal directions (see Fig. 1). The viewing directions were sampled on an evenly spaced grid in projected-cosine space: $\hat{k}_{\mathrm{r},x} = \sin\theta_\mathrm{r} \cos\phi_\mathrm{r}$ and $\hat{k}_{\mathrm{r},y} = \sin\theta_\mathrm{r} \sin\phi_\mathrm{r}$. The spacing of $\hat{k}_{\mathrm{r},x}$ and $\hat{k}_{\mathrm{r},y}$ were each 0.1, so that the angle spacing was about 5.7° near the surface normal ($\theta_\mathrm{r} = 0$) and larger at larger θ_r. Although this is a coarse grid, there were few sharp features in the scattering distribution, so it was sufficient to capture the details of the scattering behavior.

2.3 Near-retroreflective BRDF measurements

Measurements of the BRDF were also performed in a near-retroreflective geometry, simultaneously varying the incident and viewing directions. Since the detector cannot view the illuminated sample closer than about 5° from the retroreflective direction without blocking the incident radiation, the incident direction was scanned from $\theta_\mathrm{i} = 0°$ to $-75°$,

Foldyna, Martin; Germer, Thomas; Mrazkova, Zuzana.
"Mueller matrix bidirectional reflectance distribution function measurements and modeling of textured silicon surfaces."
Paper presented at SPIE Optics and Photonics, San Diego, CA. August 28, 2016 - August 29, 2016.

while the receiver was scanned from $\theta_\mathrm{r} = -5°$ to $70°$, each in steps of $1°$, maintaining a constant bistatic angle of $5°$. The results are displayed as a function of the central angle $\theta = (\theta_\mathrm{r} - \theta_\mathrm{i})/2$. These measurements were carried out scanning in the (110) crystal plane, as described before, and in the (100) crystal plane, which includes the $[0\bar{1}0]$ and $[001]$ crystal directions (see Fig. 1). Scanning in the (110) plane allows us to observe direct specular reflection from the faces of the pyramids, while scanning in the (100) plane allows us to irradiate and view the sample along the edges of the pyramids. While the measurements are performed in steps of $1°$, the goniometer and sample angles are aligned to within $0.1°$. Sharp retroreflective features are reported to a precision of $0.5°$.

2.4 Mueller matrix measurements

All of the measurements mentioned in Secs. 2.2 and 2.3 were obtained as full Mueller matrix polarimetry. The polarization state of directional radiation is characterized by a four-element Stokes vector,

$$\left(I_{\hat{\mathbf{a}}} + I_{\hat{\mathbf{b}}}, \qquad I_{\hat{\mathbf{a}}} - I_{\hat{\mathbf{b}}}, \qquad I_{\hat{\mathbf{a}}+\hat{\mathbf{b}}} - I_{\hat{\mathbf{a}}-\hat{\mathbf{b}}}, \qquad I_\mathrm{lcp} - I_\mathrm{rcp}\right)^T, \tag{2}$$

where $\hat{\mathbf{a}}$ and $\hat{\mathbf{b}}$ are unit vectors chosen to be orthogonal to each other and to the direction of propagation $\hat{\mathbf{k}}$, so that $\hat{\mathbf{a}} \times \hat{\mathbf{b}} = \hat{\mathbf{k}}$. The choice for $\hat{\mathbf{a}}$ and $\hat{\mathbf{b}}$ will be discussed below. The last element is the difference between left circular polarization (lcp) and right circular polarization (rcp). The I_q indicates a temporally- and/or spatially-averaged intensity-like quantity (*e.g.*, radiance, irradiance, radiant power, etc.), measured with an analyzer for polarization q. The choice of handedness and the signs of the second, third, and fourth elements is arbitrarily chosen, but is consistent, once that choice is made.

A Mueller matrix represents a linear relationship between two intensity-like quantities. In the context of the measurements here, the BRDF, given by Eq. (1), is the relationship between the incident radiant power, Φ_i , a Stokes vector, and the scattered radiant power, Φ_r, also a Stokes vector, and is thus a Mueller matrix. The representation of that Mueller matrix, however, depends upon the basis used for defining the Stokes vectors. [7] The choice for $\hat{\mathbf{a}}$ and $\hat{\mathbf{b}}$ in Eq. (2) is relatively straightforward for specular reflection and for measurements in the plane of incidence, since it is natural to use vectors $\hat{\mathbf{s}}$ and $\hat{\mathbf{p}}_j$, respectively, where $\hat{\mathbf{s}}$ is perpendicular to the plane of incidence, and $\hat{\mathbf{p}}_j = \hat{\mathbf{k}}_j \times \hat{\mathbf{s}}$ $(j = \mathrm{i}, \mathrm{r})$. However, in general viewing geometries out of the plane of incidence, the choice of basis is not unique. Converting Mueller matrices measured in one basis to that measured in another is straightforward. At least three such bases, which we will denote spsp, plane, and xyxy, are typically used:

- For spsp, $\hat{\mathbf{s}}_\mathrm{i}$ and $\hat{\mathbf{p}}_\mathrm{i}$ are defined perpendicular and parallel, respectively, to the plane containing the surface normal and the incident direction (the incident plane) and used for the incident direction, while $\hat{\mathbf{s}}_\mathrm{r}$ and $\hat{\mathbf{p}}_\mathrm{r}$ are likewise defined by the plane containing the surface normal and the viewing direction (the viewing plane) and used for the viewing direction. The spsp basis has an ambiguity when either the incident direction or the scattering direction lies along the surface normal, creating a basis-induced singularity in this direction.
- The plane basis uses $\hat{\boldsymbol{\sigma}}$ and $\hat{\boldsymbol{\pi}}_\mathrm{i}$ for the incident radiation and $\hat{\boldsymbol{\sigma}}$ and $\hat{\boldsymbol{\pi}}_\mathrm{r}$ for the viewing direction, where $\hat{\boldsymbol{\sigma}}$ is perpendicular to the scattering plane, defined by the incident and viewing directions, and $\hat{\boldsymbol{\pi}}_\mathrm{i}$ and $\hat{\boldsymbol{\pi}}_\mathrm{r}$ are each in the scattering plane $\hat{\boldsymbol{\pi}}_j = \hat{\mathbf{k}}_j \times \hat{\boldsymbol{\sigma}}$. The plane basis also has basis-induced singularities, namely when the incident and scattering directions are collinear. Thus, for reflective measurements, a singularity will occur in the retroreflective direction. This basis is the natural one for two different types of scattering: free space aerosols (not considered here) and simple facet scattering (discussed later). It is also the natural basis for the laboratory, since the scattering plane is fixed and horizontal.
- Finally, the xyxy basis uses vectors $\hat{\mathbf{y}}_\mathrm{i}$ and $\hat{\mathbf{x}}_\mathrm{i}$ for the incident radiation and $\hat{\mathbf{y}}_\mathrm{r}$ and $\hat{\mathbf{x}}_\mathrm{r}$ for the scattered radiation, where

$$\begin{aligned} \hat{\mathbf{y}}_j &= \hat{\mathbf{s}}_j \cos\phi_j - \hat{\mathbf{p}}_j \sin\phi_j\,, \\ \hat{\mathbf{x}}_j &= \hat{\mathbf{s}}_j \sin\phi_j + \hat{\mathbf{p}}_j \cos\phi_j\,, \end{aligned} \tag{3}$$

  which removes the basis-induced singularity along the surface normal that exists in the spsp basis. The xyxy basis is the natural laboratory basis for conoscopic, back-focal plane imaging, microscopes.

All measurements reported here were obtained as full Mueller matrices using a 4×4 measurement scheme with four incident polarization states and four polarization analysis states. These states were each achieved by rotating a retarder with one of its axes at $-45°$, $-15°$, $15°$, and $45°$ with respect to the axis of an adjacent polarizer. The data reduction matrix, which relates the sixteen measurements to the sixteen elements of the Mueller matrix, was determined using the scheme described by Compain, *et al.*, [8] using eighteen rotations of a Glan polarizer and reflection from an aluminum mirror at thirteen incident angles. The method, requiring only a single polarizer at $45°$ and a single retarder/diattenuator, was performed with much higher redundancy to improve the calibration and to provide statistics that indicate the uncertainties in subsequent measurements. The standard deviation of all of the matrix elements from their nominal values was 0.004. The mean transmittance of the polarizer was found to be 0.479 with a standard deviation of 0.009. Mueller matrix BRDFs in this paper are displayed normalized. That is, the upper left element, $f_{\mathrm{r},00}$, is shown in the natural units for BRDF, sr^{-1}, while the other elements are shown normalized, that is $m_{ij} = f_{\mathrm{r},ij}/f_{\mathrm{r},00}$.

The Gil-Bernabeu depolarization index is a measure of the degree to which a medium depolarizes radiation and is related to the Mueller matrix $\mathbf{M}$ by [9]

$$P_{\mathrm{D}} = \sqrt{[\mathrm{tr}(\mathbf{M}^{\mathrm{T}}\mathbf{M}) - M_{00}^2]/(3M_{00}^2)}. \tag{4}$$

If $P_D = 1$, the medium is non-depolarizing, while for $P_D = 0$, the medium is a total depolarizer. A lack of depolarization suggests that only one scattering path is contributing to the signal, while existence of depolarization suggests that multiple, incoherent paths are contributing to the signal.

3. SAMPLES

Three silicon samples were measured for this study. Figure 2 show a scanning electron microscope (SEM) image for each sample. Figure 2(a) shows an as-cut silicon surface, that obtained after sawing and with no polishing or etching. No visible saw marks could be observed on the surface. Figures 2(b) and 2(c) show pyramidal silicon, created by alkaline etching (KOH) of silicon with two different additives. The sample shown in Fig.2(b) had isopropyl alcohol (IPA) as an additive, while Fig. 2(c) used a commercial surfactant (RENA monoTEX[1]). These samples will be referred to as as-cut, IPA, and RT, respectively. The IPA sample has pyramids with linear dimensions about two to three times larger than those on the RT sample.

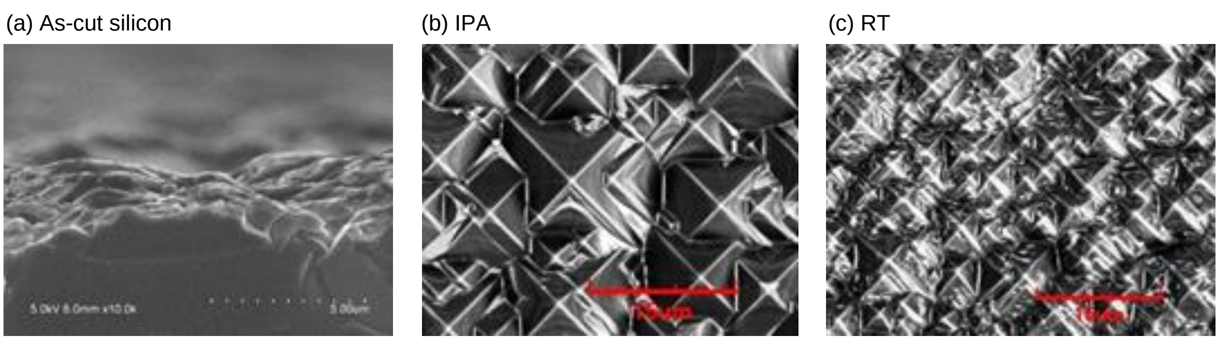

Figure 2. SEM images of the three samples used in this study: (a) as-cut silicon, (b) silicon etched with KOH and an IPA additive, and (c) silicon etched with KOH and a commercial surfactant additive. The scales of the three images are different; the bars correspond to 5 µm, 15 µm, and 15 µm, respectively. In (a) the image is a side view, while in (b) and (c), the images are top view.

[1]Certain commercial equipment, instruments, or materials are identified in this paper to foster understanding. Such identification does not imply recommendation or endorsement by the authors, their employers, or their sponsors, nor does it imply that the materials or equipment identified are necessarily the best available for the purpose.

4. MODELING METHODS

4.1 Single reflection facet model

The single reflection facet model for light scattering by a very rough surface has been commonplace in the scattering literature. The attractiveness of the model is that it is very simple to evaluate, as the BRDF is given by [10, 11]

$$f_r = \frac{P(\tan\theta_n)}{4\cos\theta_\mathrm{i}\cos\theta_\mathrm{r}\cos^4\theta_\mathrm{n}}R, \tag{5}$$

where $P(\zeta)$ is the slope distribution function, θ_n is the polar angle of a facet that specularly reflects from the incident direction to the viewing direction, and R is the reflectance of such a facet. The reflectance R is a non-depolarizing Mueller matrix that is derived from the Jones matrix for specular reflection and is most naturally expressed in the plane basis. In the retroreflection geometry, the normalized Mueller matrix should be $\mathrm{diag}(1,1,-1,-1)$, as expected for normal incidence reflection. Many models have been derived from Eq. (5), differing by having different functional forms for $P(\zeta)$. The single reflection facet model does not treat multiply reflected rays.

4.2 Monte Carlo ray tracing

The scattering by pyramidal silicon, at least at normal incidence, is dominated by multiple reflective events. Monte Carlo ray tracing code was developed for modeling the scatter and absorption from rough silicon surfaces. The code generates random realizations of one or more interfaces, directs rays at a specified incident direction, and accumulates the Mueller matrix in a global basis for each path until the ray is either reflected or transmitted from the material, or if it has lost all but a specified fraction of its original energy, or if it has interacted with a surface over a specified number of times. At each interface, the Mueller matrices for reflection and transmission are calculated in a local basis. A uniform random number generator is used to decide which path (reflection, transmission, or absorption by any films on the surface) is chosen, and the normalized Mueller matrix is multiplied by the ray's accumulated Mueller matrix. Between surface interactions, the distance traveled is used with the absorption coefficient to reduce the energy in the ray. If the ray reflects or transmits outside the material, a virtual collector accumulates the Mueller matrix. The collector discretizes the directional spectrum by collecting proportional power onto four nearest grid points in proportion to the inverse distance of the ray from the grid points. The grid points can be on an even solid angle, projected solid angle, or angle grid and the number of grid points can be chosen as needed. The total absorbed energy for unpolarized incident light is also accumulated for each layer. Any number of surfaces can be included, but for the simulations described here, since silicon does not transmit at 633 nm, only one was needed.

A wide variety of random and deterministic surfaces can be generated on a discretized grid. The surfaces can be randomized by Fourier decomposition, multiplication by random phases, and inverse Fourier restoration, if desired. Gaussian smoothening can be applied, as well, by a similar algorithm. Multiple surface functions can be added to one another. A number of surface generators specific to pyramids were developed. The one used here randomly places the top of pyramids at uniform random lateral positions and exponentially-distributed depths and chooses the highest point of all of the overlapping pyramids to determine the surface function. All surfaces are designed to be periodic, so that no vertical edge artifacts exist. One or more thin films can be applied to any of the interfaces, and their inclusion affects the reflection and transmission coefficients and absorption. Typically, 80 to 120 realizations of the surface are generated, each with 50 pyramids, and 10^4 rays used for each realization.

4.3 Diffraction

The preponderance of aligned triangular facets on the surface are expected to behave like triangular apertures. The diffraction from these triangles can be estimated by Fourier transformation of the triangular function and the result are fans extending perpendicular to the edges when the radiation is incident normal to the triangle. [12] The full-width at half-maximum of the fans is inversely proportional to the length L of the edges, roughly $0.88\,\lambda/L$ in radians. At non-normal incidence, the directions that diffraction from an edge occurs can be calculated by requiring that the projection of the incident direction onto the edge is the same as the projection of the scattered direction on that edge. That is, these directions form the locus of solutions to

$$\hat{\mathbf{k}}_\mathrm{i}\cdot\hat{\mathbf{v}} = \hat{\mathbf{k}}_\mathrm{r}\cdot\hat{\mathbf{v}}, \tag{6}$$

where $\hat{\mathbf{v}}$ is a unit vector along the edge. These diffracted directions satisfy

$$\hat{\mathbf{k}}_{\rm r} = \hat{\mathbf{v}}(\hat{\mathbf{k}}_{\rm i}\cdot\hat{\mathbf{v}}) + (\hat{\mathbf{u}}\cos\beta + \hat{\mathbf{w}}\sin\beta)\sqrt{1-(\hat{\mathbf{k}}_{\rm i}\cdot\hat{\mathbf{v}})^2}, \tag{7}$$

where $\hat{\mathbf{u}}$ and $\hat{\mathbf{w}}$ are unit vectors perpendicular to $\hat{\mathbf{v}}$ and to each other, and β parameterizes the locus. Retro-reflection (that is, when $\hat{\mathbf{k}}_{\rm r} = -\hat{\mathbf{k}}_{\rm i}$) from that edge will occur when $\hat{\mathbf{k}}_{\rm i}\cdot\hat{\mathbf{v}} = 0$, that is, when the incident radiation is perpendicular to the edge.

The angle $\alpha_{\rm e}$ that the edge of a square pyramid makes with respect to the mean surface plane is related to the angle $\alpha_{\rm f}$ of the pyramid face by $\sqrt{2}\tan\alpha_{\rm e} = \tan\alpha_{\rm f}$. A pyramid on a (001) surface of silicon and having faces consisting of (111) faces will have those faces oriented $\alpha_{\rm f} = \arctan\sqrt{2} \approx 54.7°$ from the surface normal and edges oriented at $\alpha_{\rm e} = 45°$.

Diffraction from edges may also be reflected in opposing faces. The angle at which a ray diffracts from an edge to be retro-reflected from a face, when the incident direction is in the (100) plane, is

$$\cos\alpha_{\rm r} = \frac{2\cos^2\alpha_{\rm f}}{\sqrt{-\frac{7}{2} + 6\cos 2\alpha_{\rm f} - \frac{1}{2}\cos 4\alpha_{\rm f} + 2\sec^2\alpha_{\rm f}}}. \tag{8}$$

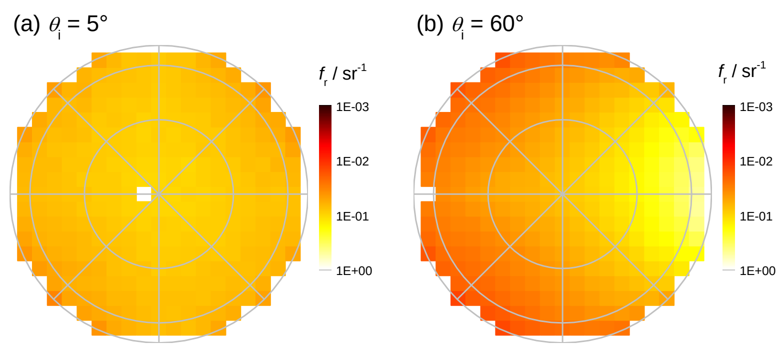

Figure 3. The BRDF measured from the as-cut silicon sample shown in direction-cosine space for incident angles (a) 5° and (b) 60°. The plane of incidence is a horizontal slice through the center. The missing point in each frame is due to the receiver blocking the incident beam. A polar grid is superimposed on the BRDF to guide the eye.

5. RESULTS AND DISCUSSION

5.1 As-cut sample measurements

Figure 3 shows the results for the hemispherical BRDF measurements for the as-cut silicon sample, with incident angles of $\theta_{\rm i} = 0°$ and 60°. The BRDF shows few features, only a broad forward scattering lobe when $\theta_{\rm i} = 60°$. There is a slight asymmetry to the scattering that is roughly aligned with the crystal axes, but a little off, presumably due to the saw direction, a propensity for a specific cleavage facet, or both. Since the reflectance $\rho = \pi\langle f_r\rangle$ when points are sampled uniformly in direction-cosine space, the reflectance of the surface can be determined from these data to be about 0.24 and 0.25 at 0° and 60°, respectively.

Figure 4 shows the normalized Mueller matrix for the as-cut silicon sample and $\theta_{\rm i} = 60°$ for the three different bases. By showing the Mueller matrix with the three bases, we demonstrate why a specific basis may be particularly advantageous for a specific scatterer. In this case, the results in the plane basis are predominantly of the form

$$\begin{pmatrix} 1 & m_{01} & 0 & 0 \\ m_{01} & 1 & 0 & 0 \\ 0 & 0 & m_{22} & m_{23} \\ 0 & 0 & -m_{23} & m_{22} \end{pmatrix}. \tag{9}$$

Foldyna, Martin; Germer, Thomas; Mrazkova, Zuzana.
"Mueller matrix bidirectional reflectance distribution function measurements and modeling of textured silicon surfaces."
Paper presented at SPIE Optics and Photonics, San Diego, CA. August 28, 2016 - August 29, 2016.

This form is expected when the material is non-depolarizing and when the Jones matrix is diagonal. Furthermore, the m_{23} and m_{32} elements are weak when the phase between the Jones matrix elements is small. Thus, in the context of this measurement, the plane basis is the natural basis for the scattering from this sample. As for the other bases, there is a singularity in the Mueller matrix in the spsp basis that dominates the appearance of that matrix. No singularities are observed in the xyxy basis set, but the form of the matrix is more complicated than Eq. (9). The singularity that exists in the plane basis, seen along the plane of incidence, to left of the center of the graphs, in the retroreflective direction, is at a point where the Mueller matrix is very nearly diagonal (the off-diagonal elements all show nearly white in this region), and is very weak for this sample. While weak, it is most observable in the m_{13} and m_{31} elements, and to an even lesser degree, the m_{23} and m_{32} elements.

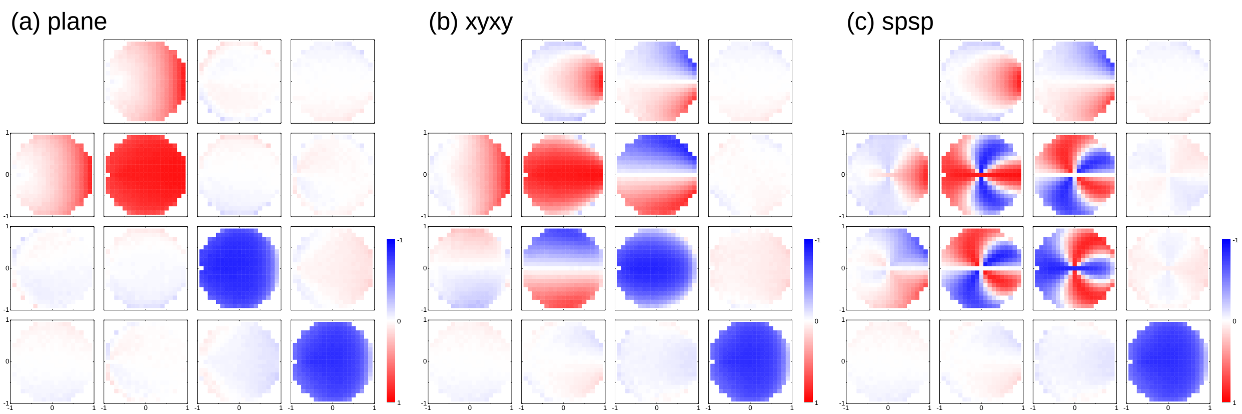

Figure 4. The normalized Mueller matrix for scattering from the as-cut silicon sample for three different bases measured with an incident angle $\theta_{\mathrm{i}} = 60°$. The bases are (a) plane, (b) xyxy, and (c) spsp.

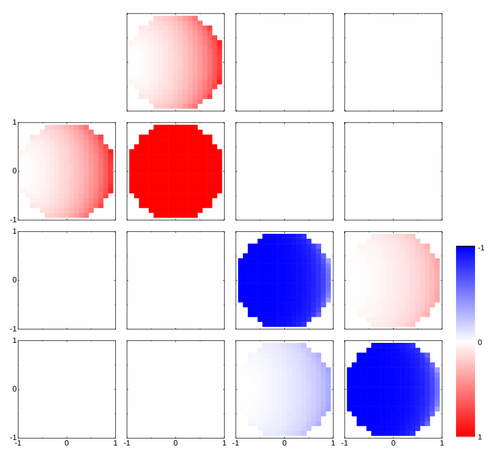

Figure 5. The simulated normalized Mueller matrix elements in the plane basis for a rough silicon surface in the single reflection microfacet approximation with $\lambda = 633$ nm and $\theta_{\mathrm{i}} = 60°$. A 20 nm Bruggeman effective medium approximation 1:1 mix of silicon and vacuum was included in the simulation.

That the plane basis nearly diagonalizes the Jones matrix is not universal to surface scattering. However, it is the natural basis for the single reflection facet scattering model. In Fig. 5, we show a simulation using the facet model, where we have included a thin effective medium approximation layer, which is necessary to simulate the observed behavior in m_{23} and m_{32}. It is worth noting that, within the facet approximation, the Mueller matrix is not a function of the slope distribution. The agreement between the simulation (Fig. 5) and the measurement [Fig. 4(a)] is reasonable. As mentioned above, the small deviations and especially the observation of the weak singularity in elements m_{13}, m_{31}, m_{23}, and m_{32} suggest that other effects, such as multiple scattering and diffraction, play a minor role.

Figure 6 shows the near-retroreflection measurement results for the as-cut silicon sample. It is observed that the scatter is higher and has a broad shoulder in the (110) plane, in comparison to measurements in the (100) plane. Whether these results are indicative of residual saw marks or whether they are due to a preference for facets aligned along the (111) cleavage plane is unknown. The shoulder in the (110) retroreflection measurements, while being centered near the 54.7° angle, is too broad to make this assignment conclusive.

Figure 6 also shows the block-diagonal elements of the Mueller matrix in retroreflection. The off-block-diagonal elements are all zero within the expected uncertainties and are not shown. If the retroreflection signal were completely dominated by single reflection, the Mueller matrix would indicate normal incidence reflection and be $\mathrm{diag}(1,1,-1,-1)$. While the matrix is close to this, especially in the (110) plane, clear deviations can be observed. These deviations are probably from the minor role that multiple scattering and diffraction are expected to play.

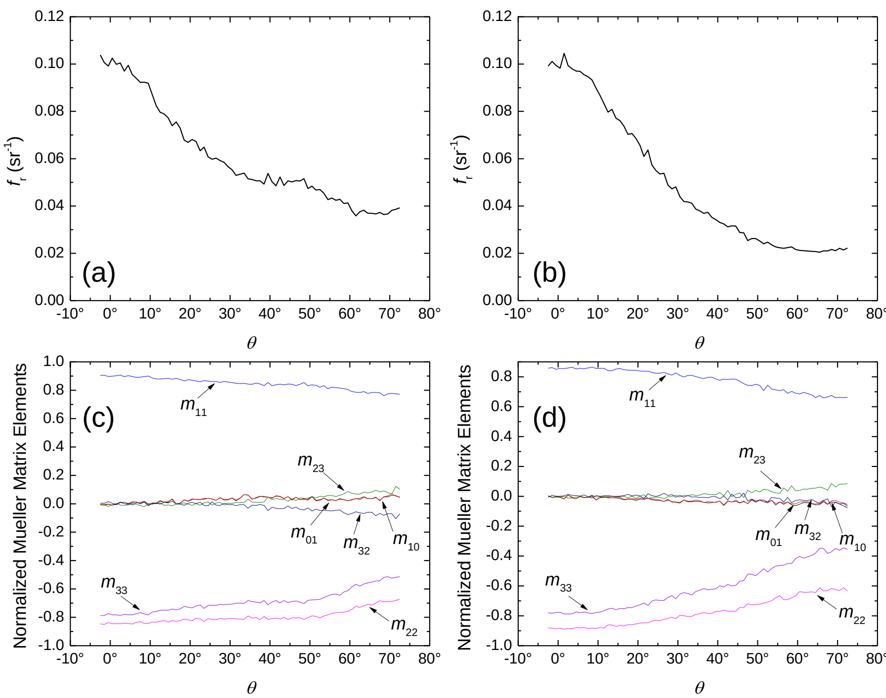

Figure 6. The results from near-retroreflection measurements from the as-cut silicon sample as functions of the center angle: the BRDF measured in (a) the (110) plane, and (b) the (100) plane, and the normalized Mueller matrix elements measured in (c) the (110) plane, and (d) the (100) plane. Only the block-diagonal Mueller matrix elements are shown; the off-block elements are very close to zero.

While the plane basis is particularly interesting for the as-cut silicon sample, the block-diagonal behavior in that basis was unique to that sample. In the remainder of this paper, we will only show data in the xyxy basis, since it has the fewest basis-induced artifacts. No diagonalization in the plane basis was observed for the pyramidal silicon samples.

5.2 Pyramidal silicon sample measurements

Figure 7 shows the unpolarized BRDF (the $f_{\mathrm{r},00}$ Mueller matrix element) for the pyramidal silicon samples for 5° and 60° incident angles. Both samples show significantly more structure than the as-cut sample. At $\theta_{\mathrm{i}} = 5°$ the IPA sample shows four clear peaks. These four peaks, marked A, B, and C, arise from double reflections from the faces of neighboring pyramids (see key on right of Fig. 7). The breaking of the symmetry (that the two out-of-plane peaks, marked C, move to the right, while the two in-plane peaks, marked A and B move to the left, as shown) is predicted by the multiple reflection model, and the peaks are roughly where they are expected. However, close inspection reveals that they are closer together than expected from (111) facets. At $\theta_{\mathrm{i}} = 60°$, there is a very strong back reflection (shown saturated in the figure at D) that is expected from the direct reflection from the pyramid faces. In the forward scattering direction, just off the plane of incidence, there are two distinct, but relatively weak peaks marked C, which correspond to a double reflection and which evolved from the out-of-plane peaks observed at $\theta_\mathrm{i} = 5°$. Most striking in the $\theta_\mathrm{i} = 60°$ data is the band of radiation in out-of-plane directions starting from the feature D. This latter band can be best assigned to diffraction from the edges of the triangular faces of the pyramids. Superimposed on the $\theta_\mathrm{i} = 60°$ data in Fig. 7 are curves showing the expected directions from such diffraction. Also, the expected locations of other doubly reflected rays (E and F) are shown with the key to their assignments. The angles used for calculating the diffraction curves and the locations of the rays are taken from the retroreflection measurements described below.

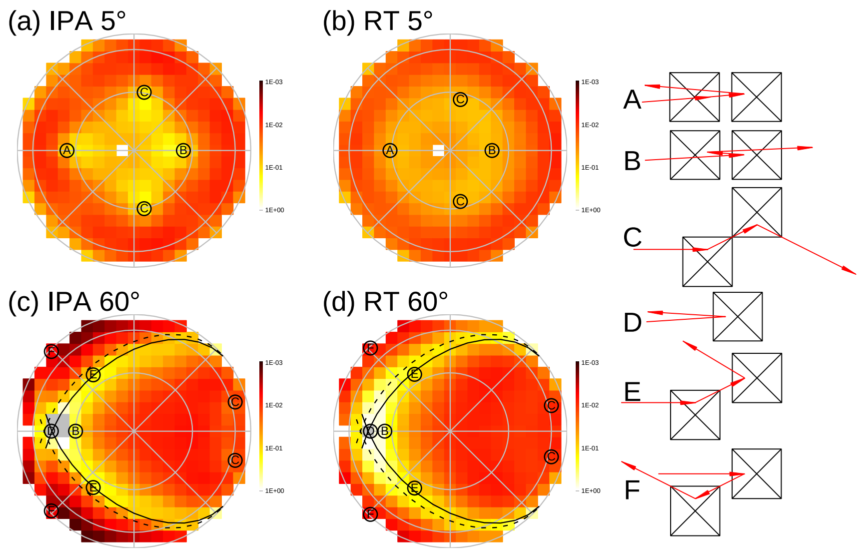

Figure 7. The BRDF measured from the pyramidal silicon samples shown in direction-cosine space for (a) and (c) the IPA sample and (b) and (d) the RT sample. The incident angles were (a) and (b) $\theta_\mathrm{i} = 5°$ and (c) and (d) $\theta_\mathrm{i} = 60°$. The plane of incidence is a horizontal slice through the center. Superimposed upon the BRDF data are expected locations for diffraction from edges with angles (solid curves) 42.5° and (dashed curves) 45.5°, and (circles with letters, key on the right) single and double reflections. Also superimposed on the BRDFs are polar grids to guide the eye.

Figure 8 shows the near retro-reflection behavior of the pyramidal silicon samples. In the (110) plane, a sharp peak is observed for the IPA sample, centered on the angle $\theta = 52.5°$. This peak can be readily assigned to the normal reflection of pyramid faces. That this angle differs from the orientation of (111) crystal faces (54.7°) is consistent with other findings that the faces of the pyramids formed by alkali etching are close to, but not exactly, (111) faces. [4, 13] There is also a broad peak near 12°; this peak is believed to be a combination of a number events, including a three-reflection, enhanced backscatter event.

When measuring the near-retro-reflection from the IPA sample in the (100) plane, shown in Fig. 8(b), there are two distinct peaks at 36.5° and 42.5°. These features cannot be correlated with any expected reflections from (111) or near-(111) facets. Instead, we find that they require diffraction to understand. In particular, the peak at $\theta = 42.5°$ matches well to the edge angle of the pyramids, which would be 42.7° for pyramids having faces oriented at 52.5°. Thus, the $\theta = 42.5°$ feature is assigned to diffraction from the pyramid edges. The $\theta = 36.5°$ feature is likely to be a combination of diffraction from an edge and reflection from a pyramid face. Such a reflection and diffraction combination depends strongly on the pyramid angle α_f [see Eq. (8)]. Thus, for $\alpha_\mathrm{f} = 52.5°$ (the value determined for the pyramid angle above), 53.2°, and 54.7° (the ideal pyramid), retro-reflection will occur at $\theta = 32.8°$, 36.5° (the value from above), and 45°, respectively. Thus, we believe that this assignment lies within the anticipated resolution of the measurement ($\approx 1°$ due to sampling spacing).

We notice that the intensity of the 36.5° feature is higher than the 42.5° feature. Because it is a multiple scattering event, *i.e.*, a face reflection and an edge diffraction, it is subject to enhanced backscattering. [14] That is, in the retroreflection direction, the path lengths of the forward and reversed paths coincide, so that the fields coherently add. Thus, even though the extra reflection might be expected to reduce the reflectance, the backscattering effect might be enhancing it.

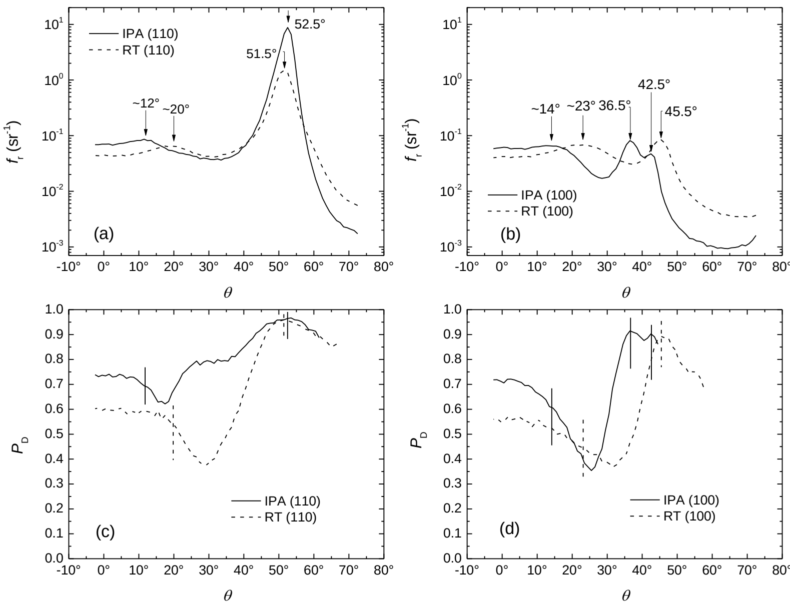

Figure 8. The results from near-retroreflection measurements from the (solid) IPA sample and (dashed) RT sample as functions of the center angle, with (a) and (b) the BRDF and (c) and (d) the depolarization index, measured in (a) and (c) the (110) plane and (b) and (d) the (100) plane. Vertical marks in (c) and (d) are at the same angles as the feature labels in (a) and (b), respectively.

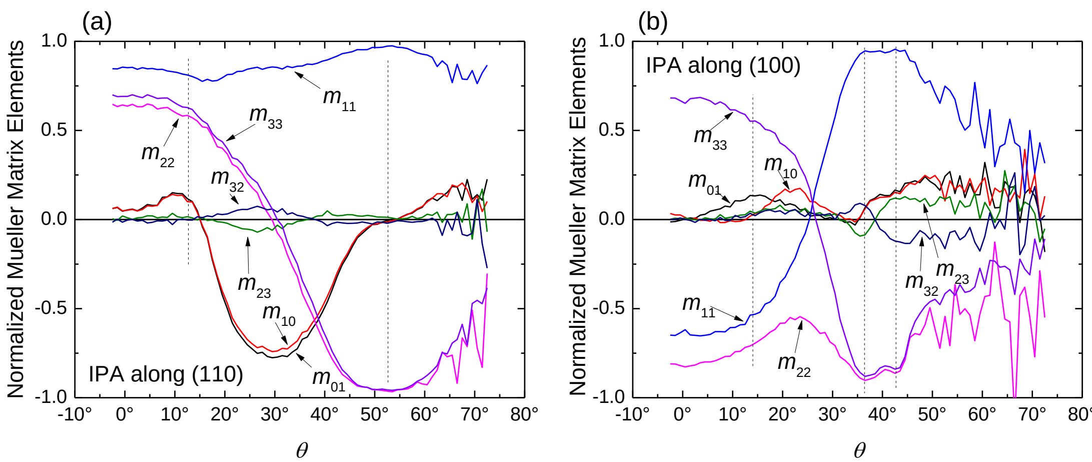

Figure 9. Normalized Mueller matrix elements measured for the IPA sample in the near-retroreflection geometery in (a) the (110) plane and (b) the (100) plane. The vertical marks are aligned with features observed for the IPA sample in Fig. 8.

Figure 8 also shows the depolarization index P_D for the near-retroreflection measurements. At the locations of the assigned higher angle peaks mentioned above, the depolarization index is high, as expected for simple deterministic scattering events. At the lower angle peak, the depolarization index is significantly lower and does not peak at the same angles as peaks in the intensity, suggesting that the origin of these features is significantly more complicated. Figure 9 shows the block diagonal Mueller matrix elements for the same data shown in Fig. 8. For measurements in the (110) plane, the matrix has approximately the behavior observed in Eq. (9) (the off-block-diagonal matrix elements are zero and not shown). The feature at $52.5°$ shows values close to $\mathrm{diag}(1,1,-1,-1)$, consistent with normal incidence reflection from the pyramid facets. For measurements in the (100) plane, the matrix is still block diagonal. While the matrix at both 36.5° and 42.5° features follow the form of Eq. (9), the elements m_{23} and m_{32} flip sign between them. At the lower angle

Foldyna, Martin; Germer, Thomas; Mrazkova, Zuzana.
"Mueller matrix bidirectional reflectance distribution function measurements and modeling of textured silicon surfaces."
Paper presented at SPIE Optics and Photonics, San Diego, CA. August 28, 2016 - August 29, 2016.

features, however, there is a marked difference between m_{10} and m_{01}. Such asymmetries in the Mueller matrix have been observed in the past in the presence of significant depolarization and indicate the presence of depolarization before or after the other scattering events. [15]

Figures 7 and 8 also show the hemispherical BRDF and the near-retroreflection measurements for the RT sample. The unpolarized BRDF shows a number of differences from the IPA sample. At $\theta_\mathrm{i} = 5°$, the four peaks observed for the IPA sample have disappeared and been replaced by a broad doughnut, while at $\theta_\mathrm{i} = 60°$, the feature assigned to diffraction from the pyramid edges is also broader and has shifted to higher polar angles. The broadening of the features is not surprising, since from Fig. 2 the pyramid dimensions are much smaller.

In the near-retroreflection measurements, the RT sample has somewhat different results than the IPA sample. In the (110) plane, the main peak is significantly reduced in intensity and shifted to a slightly lower angle, $\theta = 51.5°$, while the low angle peak has shifted to a higher angle, about 20°. In the (100) plane, there are only two features at about 23° and 45.5°. It is difficult to reconcile the assignments of these angles with simple pyramids. The feature at 45.5° is very close to the value expected for a (111)-faceted pyramid. Furthermore, the diffraction curve observed in the hemispherical data is closer to that expected for 45.5° edges [see dashed curves in Fig. 7(d)]. This suggests that the edges are well aligned with the [101] direction. However, the direct retro-reflection suggests that the faces have a shallower angle than the (111) faces. These results suggest that the RT sample pyramids are more complex, perhaps having multiple facets, such as octagonal pyramids, or even curved faces. Such features have been observed in the past.[13, 16]

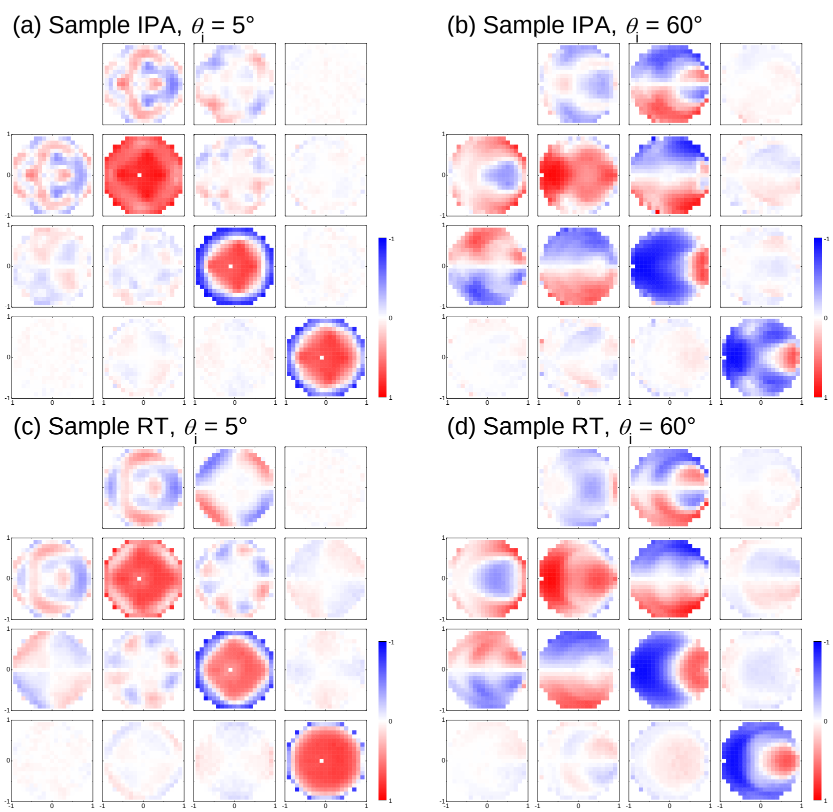

Figure 10. Normalized Mueller matrix in the xyxy basis measured for (a) and (b) sample IPA and (c) and (d) sample RT. The incident angles were (a) and (c) 5° and (b) and (d) 60°.

Figure 10 shows the normalized Mueller matrices for both the IPA and the RT samples for both incident angles. As mentioned above, we use the xyxy basis to show the matrices, since there are no basis-induced artifacts and we did not observe any evidence for diagonalization by using the plane basis. Both samples show quite a bit of structure, which is not surprising, given the number of different reflection and diffraction features that are present. In general, the two samples

Foldyna, Martin; Germer, Thomas; Mrazkova, Zuzana.
"Mueller matrix bidirectional reflectance distribution function measurements and modeling of textured silicon surfaces."
Paper presented at SPIE Optics and Photonics, San Diego, CA. August 28, 2016 - August 29, 2016.

have similar Mueller matrices for each angle, although those for the RT sample are much smoother and less distinct than those of the IPA sample. It is interesting to note that, while one has difficulty observing the double-reflection peaks in the unpolarized BRDF of the RT sample, one can see vestiges of those peaks in the Mueller matrix for $\theta_\mathrm{i} = 5°$.

Modeling was carried out to attempt to simulate the observed Mueller matrices. Since the models described above do not include diffraction, it is difficult to simulate the Mueller matrices over the hemisphere. However, we made a number of approximations that attempt to mimic the effects of diffraction. In particular, if we start with a pyramidal structure, smoothening the surface will cause the edges to round off in a manner that will reflect in directions that have a similar requirement as Eq. (5). Secondly, by adding some random roughness, we can simulate the natural broadening that will occur due to diffraction from the finite size of the pyramid faces. Figure 11 shows the results of these simulations. In must be stressed that these are not rigorous models and are just attempts to empirically capture the behavior of the observed Mueller matrices. While some features in the Mueller matrix are mimicked well, there are a number of features that were difficult to replicate. In particular, it is found that features in the last row and last column (except where they coincide, m_{33}), appear to have the wrong sign. While an effective medium layer was used to simulate subwavelength roughness (otherwise these elements would be negligible), it was found that the sign of these elements could only be simulated if the effective medium had a *higher* index than the bulk material. While a poor result may be expected in those scattering directions that are dominated by diffractive effects, it is somewhat surprising that the modeling does not replicate the measured behavior at the double-reflection features labeled C in Fig. 7(c).

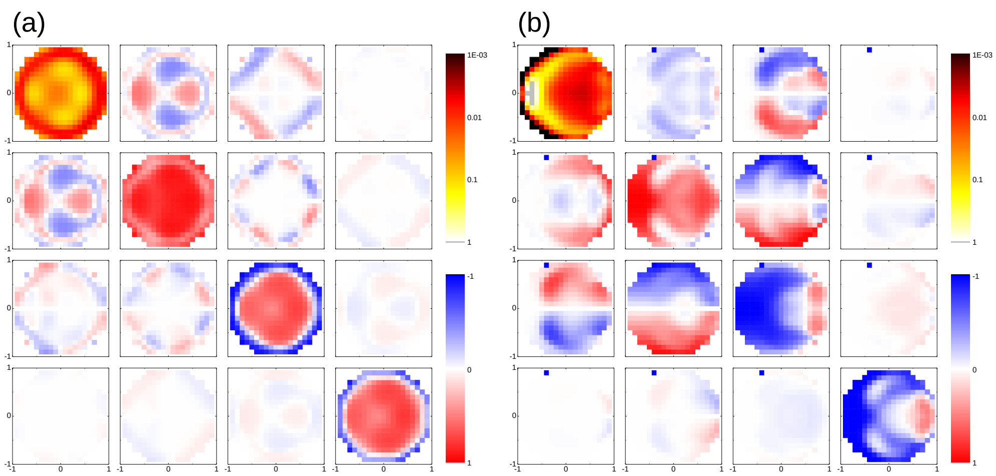

Figure 11. Modelled BRDF and normalized Mueller matrix for a pyramidal silicon as described in the text. The incident angles were (a) 5° and (b) 60°.

6. CONCLUSIONS

These measurements demonstrate some of the strengths as well as weaknesses of using light scattering to characterize rough surfaces. The additional information provided by the Mueller matrix helps to identify the sources of light scattering and guides the researcher into applying an appropriate model. Additionally, the use of full hemispherical scans highlights anisotropic features in the material. Retroreflection measurements can be used to infer the slope distribution of the surface, and polarimetry provides a verification or rejection of that interpretation. In the case of the textured silicon surfaces measured in this study, some details of the surface pyramids were able to be deduced from the light scattering measurements. However, the results shown here also demonstrate the limitations of the scattering models. In particular, it was found that diffraction plays an important role in these materials. It is clear that models need to be developed that can be applied to large scale roughness, but which also include the diffractive nature of scattering. That is particularly difficult in these materials, since not only the lateral distances are large, the vertical distances are, too. The information gained from these measurements should prove useful for the development of photovoltaics.

Foldyna, Martin; Germer, Thomas; Mrazkova, Zuzana.
"Mueller matrix bidirectional reflectance distribution function measurements and modeling of textured silicon surfaces."
Paper presented at SPIE Optics and Photonics, San Diego, CA. August 28, 2016 - August 29, 2016.

REFERENCES

[1] P. Campbell and M. A. Green, "Light trapping properties of pyramidally textured surfaces," J. Appl. Phys. **62**, 243-249 (1987).

[2] E. Yablonovitch, "Statistical ray optics," J. Opt. Soc. Am. **72**, 899-907 (1982).

[3] E. Yablonovitch and G. D. Cody, "Intensity Enhancement in Textured Optical Sheets for Solar Cells," IEEE Trans. Electron Devices **ED-29**, 300-305 (1982).

[4] E. Forniés, C. Zaldo and J. M. Albella, "Control of random texture of monocrystalline silicon cells by angle-resolved optical reflectance," Solar Energy Materials and Solar Cells **87**, 583-593 (2005).

[5] H. Mäckel, D. M. Cambre, C. Zaldo, J. M. Albella, S. Sánchez, C. Vázquez, I. Sánchez and M. Á. Vásquez, "Characterization of monocrystalline silicon texture using optical refelctance patterns," in *23rd European Photovoltaic Solar Energy Conference and Exhibition*, Valencia, Spain, pp. 1160-1163 (2008).

[6] T. A. Germer and C. C. Asmail, "Goniometric optical scatter instrument for out-of-plane ellipsometry measurements," Rev. Sci. Instr **70**, 3688-3695 (1999).

[7] N. Trouve, E. Colin-Koeniguer, P. Fargette and A. De Martino, "Influence of Geometrical Configurations and Polarization Basis Definitions on the Analysis of Bistatic Polarimetric Measurements," IEEE Transactions on Geoscience and Remote Sensing **49**, 2238-2250 (2011).

[8] E. Compain, S. Poirier and B. Drevillon, "General and self-consistent method for the calibration of polarization modulators, polarimeters, and Mueller-matrix ellipsometers," Appl. Opt **38**, 3490-3502 (1999).

[9] J. J. Gil and E. Bernabeu, "Depolarization and polarization indices of an optical system," Optica Acta **33**, 185-189 (1986).

[10] D. E. Barrick, "Rough surface scattering based on the specular point theory," IEEE Trans. Ant. Prop **AP-16**, 449-454 (1968).

[11] K. E. Torrance and E. M. Sparrow, "Theory of off-specular reflection from roughened surfaces," J. Opt. Soc. Am **57**, 1105-1114 (1967).

[12] R. C. Smith and J. S. Marsh, "Diffraction patterns of simple apertures," J. Opt. Soc. Am. A **64**, 798-803 (1974).

[13] J. D. Hylton, A. R. Burgers and W. C. Sinke, "Alkaline Etching for Reflectance Reduction in Multicrystalline Silicon Solar Cells," J. Electrochem. Soc **151**, G408-G427 (2004).

[14] Y. N. Barabanenkov, Y. A. Kravtsov, V. D. Ozrin and A. I. Saichev, "Enhanced Backscattering in Optics," Progress in Optics **29**, 65-197 (1991).

[15] T. A. Germer and H. J. Patrick, "Mueller matrix bidirectional reflectance distribution function measurements and modeling of diffuse reflectance standards," in *Polarization Science and Remote Sensing V,* edited by J. A. Shaw and J. S. Tyo, Proc. SPIE **8160**, 81600D (2011).

[16] S.-S. Tan, M. L. Reed, H. Han and R. Boudreau, "Mechanisms of Etch Hillock Formation," J. Microelectromech. Sys. **5**, 66-72 (1996).